

BATTERIES

Solvent-mediated oxide hydrogenation in layered cathodes

Gang Wan^{1,2}*, Travis P. Pollard³, Lin Ma^{3,4}, Marshall A. Schroeder³, Chia-Chin Chen⁵, Zihua Zhu⁶, Zhan Zhang⁷, Cheng-Jun Sun⁷, Jiyu Cai⁸, Harry L. Thaman⁹, Arturas Vailionis^{10,11}, Haoyuan Li², Shelly Kelly⁷, Zhenxing Feng¹², Joseph Franklin^{13,14}, Steven P. Harvey¹⁵, Ye Zhang¹⁶, Yingge Du¹⁷, Zonghai Chen⁸, Christopher J. Tassone¹, Hans-Georg Steinrück^{1,18,19,20}, Kang Xu^{3,21}*, Oleg Borodin³*, Michael F. Toney^{1,22}*

Self-discharge and chemically induced mechanical effects degrade calendar and cycle life in intercalation-based electrochromic and electrochemical energy storage devices. In rechargeable lithium-ion batteries, self-discharge in cathodes causes voltage and capacity loss over time. The prevailing self-discharge model centers on the diffusion of lithium ions from the electrolyte into the cathode. We demonstrate an alternative pathway, where hydrogenation of layered transition metal oxide cathodes induces self-discharge through hydrogen transfer from carbonate solvents to delithiated oxides. In self-discharged cathodes, we further observe opposing proton and lithium ion concentration gradients, which contribute to chemical and structural heterogeneities within delithiated cathodes, accelerating degradation. Hydrogenation occurring in delithiated cathodes may affect the chemomechanical coupling of layered cathodes as well as the calendar life of lithium-ion batteries.

oupled ion-electron transfer is a fundamental process that has been adapted in the switching of physical properties (1, 2), catalysis (3), and energy storage (4-6). In electrochemical energy storage devices, such as lithium-ion batteries (LIBs), the Li⁺ intercalation is coupled to electron transfer when energy is converted from chemical into electrical forms (5, 7, 8). LIBs continue to face the challenge of voltage and capacity fading over time. In particular, the charged (delithiated) state of cathodes has been investigated as one of the main sources of degradation upon cycling (5, 9-11). Beyond cycle life reduction, when a charged device is stored, the cell voltage decays, and capacity fades over time (5, 12). This self-discharge process reduces the stored energy from the (de)lithiation reaction and limits electrochemical performance. Self-discharge is a general phenomenon experienced by all rechargeable electrochemical devices (5, 12, 13). Identifying the ion-electron transfer pathways that drive self-discharge is essential to improving device performance.

To improve the energy density of LIBs, efforts have been made to explore cathode compositions with higher voltages (8, 14). Over the past three decades, the cathode voltage has risen by around 0.3 V, progressing from

LiCoO₂ (4.2 V) to LiNi_{0.5}Mn_{0.3}Co_{0.2}O₂ (NMC532), LiNi_{0.8}Mn_{0.1}Co_{0.1}O₂ (NMC811), and Li-rich layered cathodes (4.5 V). However, cathode degradation in carbonate electrolytes remains a critical limitation for both cycle and calendar life (15). The predominant understanding of cathode failure mechanisms in LIBs is mostly based on transition metal (TM) dissolution (15), interphase instability (5, 16), and chemically induced mechanical effects (chemo-mechanics) (17). This includes the buildup of mechanical stress owing to the intraparticle inhomogeneity in lithiation states or the formation of reduced phase on the cathode surface (9, 17). A voltage drop of a few hundred millivolts is commonly observed for charged lithium nickel manganese cobalt oxide (NMC) cathodes during storage over the course of hundreds of hours at open circuit voltage (OCV) (12). OCV drops become more severe when the cell is charged to higher voltages, charged at faster rates, cycled repeatedly, or operated at elevated temperatures (5, 12, 18). Our prevailing understanding of self-discharge in LIBs implicates the diffusion of Li⁺ from the electrolyte into the cathode along with the unwanted side reactions between the electrode and the electrolyte (5, 18).

Typical LIB electrolytes consist of lithium salts dissolved in carbonate solvents (5, 16).

Theoretical predictions, however, suggest that electrolyte oxidation can occur through dehydrogenation (5, 19-23). In the context of exposure to aqueous electrolytes or atmospheric moisture at high temperature or high humidity (24-26), protons (H+) are available and can substitute on the Li⁺ lattice site in layered cathodes, such as LiNiO2 and LiCoO2. These studies suggest that other coupled ion-electron behaviors, such as hydrogen (H) transfer from carbonate solvents to layered cathodes, may occur in LIBs and thus call for the elucidation of this behavior to lay the foundation for better LIB diagnosis, including self-discharge. We bridge the knowledge gap between the degradation of electrolytes and the dynamic redox behavior and bulk properties change of cathodes by combining synchrotron x-ray methods and depth-profile mass spectroscopic studies with theoretical analysis and modeling. Our study shows that interfacial hydrogen transfer occurs from the carbonate solvents to the delithiated NMC cathodes. This hydrogen transfer triggers cathode hydrogenation, which results in self-discharge and may contribute to chemo-mechanical coupling of cathodes.

Self-discharge and the interfacial hydrogen transfer

Self-discharge phenomena were first evaluated in NMC532/Li cells with LP57 electrolyte [1 M LiPF₆ in ethylene carbonate (EC)-ethyl methyl carbonate (EMC), 3:7 by weight]. The cells were charged to three different voltages and then rested for >400 hours while the cell OCVs were monitored (Fig. 1A and fig. S1). The OCV drops are potential dependent, ranging from a 50-mV drop at the 4.1-V cutoff to a 140-mV drop at the 4.5-V cutoff. This self-discharge phenomenon also leads to the additional first cycle capacity loss, which increased from around 2% at the 4.1-V and 4.3-V cutoffs to about 8.5% at the 4.5-V cutoff (Fig. 1B and materials and methods). Near-edge x-ray absorption fine structure (NEXAFS) was used to reveal the evolution of TM oxidation states in self-discharged NMC532 electrodes. Figure 1C shows the absorption peaks in Ni L₃-edge NEXAFS, corresponding to the 2p_{3/2}-to-3d transition (27), with minor changes to Co and negligible changes to Mn (fig. S2). The signals

¹SLAC National Accelerator Laboratory, Menlo Park, CA 94025, USA. ²Department of Mechanical Engineering, Stanford University, Stanford, CA 94305, USA. ³Battery Science Branch, Energy Science Division, Army Research Directorate, DEVCOM Army Research Laboratory, Adelphi, MD 20783, USA. ⁴Department of Mechanical Engineering and Engineering Science, The University of North Carolina at Charlotte, Charlotte, NC 28223, USA. ⁵Department of Chemical Engineering, National Taiwan University, Taipei 10617, Taiwan. ⁶Environmental Molecular Sciences Laboratory, Pacific Northwest National Laboratory, Richland, WA 99354, USA. ⁷Advanced Photon Source, Argonne National Laboratory, Lemont, IL 60439, USA. ⁸Chemical Science and Engineering Division, Argonne National Laboratory, Lemont, IL 60439, USA. ⁸Department of Materials Science and Engineering, Stanford University, Stanford, CA 94305, USA. ¹⁰Department of Physics, Kaunas University of Technology, LT-51368 Kaunas, Lithuania. ¹²School of Chemical, Biological, and Environmental Engineering, Oregon State University, Corvallis, OR 97331, USA. ¹³Lawrence Berkeley National Laboratory, Berkeley, CA 94720, USA. ¹⁴Department of Chemical Engineering, University College London, London WCIE 6BT, UK. ¹⁵National Renewable Energy Laboratory, Golden, CO 80401, USA. ¹⁶Department of Electrical and Computer Engineering and Materials Science and Engineering Program, University of Houston, Houston, TX 77204, USA. ¹⁷Physical and Computational Sciences Directorate, Pacific Northwest National Laboratory, Richland, WA 99354, USA. ¹⁸Department Chemie, Universitàt Paderborn, 33098 Paderborn, Germany. ¹⁹Institute for a Sustainable Hydrogen Economy, Forschungszentrum Jülich GmbH, Marie-Curie-Straße 5, 52428 Jülich, Germany. ²⁰RWTH Aachen University, Institute of Physical Chemistry, Landoltweg 2, 52074 Aachen, Germany. ²¹SES Al Corporation, Woburn, MA 01801, USA. ²²Department of Chemical and Biological Engineering, Materials Science and Engineering Program, Renewabl

were collected in two modes-total fluorescence yield (TFY) with a probing depth of around 100 nm and total electron yield (TEY), which is sensitive to <10 nm of the particle surface (27). With increasing charging potentials, the TFY spectral feature shifted toward higher photon energy, indicating a continuous Ni oxidation upon delithiation (Fig. 1C), as expected. The near-surface TEY spectral feature shifted to lower energy for all charging potentials, showing that Ni is more reduced on the surface compared with the bulk (Fig. 1D). Surface reduction of Ni is more pronounced at higher cutoffs. A similar surface-to-bulk oxidation state difference has been observed on other delithiated layered cathodes (9, 27, 28). including NMC811. The estimated time constants from the chemical diffusion of Li⁺ within the NMC532 particle are far shorter than the observed relaxation time (supplementary text), which indicates that the observed OCV drops are not exclusively attributable to the chemical diffusion of Li+. Beyond NMC532 and an LP57 electrolyte, similar OCV drop and capacity fade were observed in NMC811 using EC and diethyl carbonate (DEC) as solvents (fig. S3), which suggests generality for this phenomenon. Selfdischarge was further evaluated in a full lithiumion cell NMC532/graphite (fig. S4), demonstrating the validity and applicability of our results on NMC532/Li cells.

To understand the chemical origins of the surface reduction layer, Li_{0.7}Ni_{0.5}Mn_{0.3}Co_{0.2}O₂ (mimicking a high state of charge) and LiNi_{0.5} Mn_{0.3}Co_{0.2}O₂ films (pristine state) were prepared by pulsed laser deposition (figs. S5 and S6 and materials and methods) and soaked in LP57 electrolyte and EC-EMC solvents (3:7 by weight) without LiPF₆ salt for 2 hours in a glovebox. The oxidation states of Ni on the film surface were probed using x-ray absorption near-edge structure (XANES) in a total reflection geometry. After soaking in LP57, the Ni K-edge spectrum of $Li_{0.7}Ni_{0.5}Mn_{0.3}Co_{0.2}O_2$ shifted negatively toward that of LiNi_{0.5}Mn_{0.3} Co_{0.2}O₂ (Ni^{2.4+}; Fig. 2A). Relative to the pristine composition, Co was also reduced, whereas the Mn oxidation state remained almost unchanged (fig. S7). This aligns well with the observation of surface reduction in the LiCoO₂ film (29). The Ni was reduced throughout the entire 10-nm film, as revealed by XANES with a deeper penetration depth using an incidence angle of 10° (fig. S8). Even without the salt, exposure to the EC-EMC solvent mixture caused a similar Ni reduction, showing that the reduction is mainly driven by the carbonate solvent. Furthermore, the LiNi_{0.5}Mn_{0.3}Co_{0.2}O₂ film is found to be chemically stable with LP57 electrolyte with no observed shifts in XANES spectra (Fig. 2B and fig. S7). Therefore, the Ni reduction is the result of the chemical reaction between the delithiated (i.e., high state of charge) cathode and the carbonate solvents.

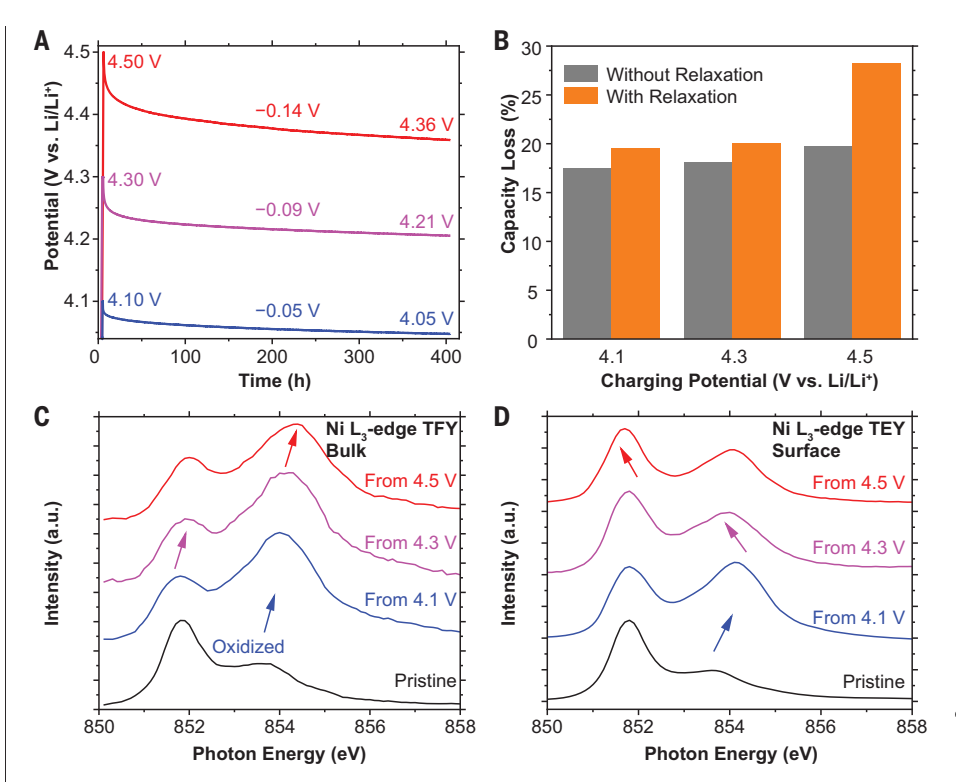


Fig. 1. Potential-dependent self-discharge of NMC532 electrodes and Ni oxidation states evolution in bulk and on the cathode surface. (A) Voltage-time profiles of OCV drop in commercial NMC532 electrodes after a galvanostatic charging to 4.1 V, 4.3 V, and 4.5 V at a rate of 0.25 C using LP57 electrolyte. (B) Capacity loss from the first charge-discharge cycle with and without 400 hours of relaxation (at OCV) (C and D) XAS of pristine NMC532 and self-discharged electrodes from different potentials collected in bulk-sensitive TFY (C) and surface-sensitive TEY (D) at the Ni L₃-edge. The right and left pointing arrows indicate the oxidation and reduction of Ni, respectively, a.u., arbitrary units.

Density functional theory (DFT) calculations were used to investigate the thermodynamic origins of the decomposition of carbonate solvents, EC and EMC, on the NMC532 (018) surface with different lithiation states. We observe that both EC and EMC can transfer either one or two H atoms to the cathode surface (Fig. 2, C and D, and fig. S9). The two-H transfer mechanism has been less explored in the literature, but we show that two-H transfer can result in the formation of vinylene carbonate (VC) or methyl vinyl carbonate. To provide further theoretical support for this observation, we turn to the average bond dissociation energy (BDE) as a good indicator of the C-H bond stability. H transfer is more favorable in molecules with a smaller BDE. The substantial difference in BDE between vinvl C-H bonds (464 kJ/mol) and methylene groups (about 370 kJ/mol) supports the proposed two-H transfer mechanism forming vinyl groups (30). Methylene groups (CH₂) can be found in both EC and EMC molecules (fig. S10). The dehydrogenation of CH₂ in EMC is more favorable compared with that in EC (fig. S9E) and is consistent with the lower dehydrogenation free energies computed in several solvation conditions (figs. S10 and S11). Based on the TM-mediated H transfer theory (31), the lattice oxygen in partially delithiated NMC532 cathode will be protonated, whereas the electron would reduce the highvalence Ni on adjacent lattice sites. Furthermore, our DFT studies show that H transfer is less favorable on the lithiated NMC532 surface (fig. S9, A and B), confirming that the interfacial H transfer from solvent to cathode requires the delithiation of the cathode oxide.

Solvent-mediated cathode hydrogenation and its importance

Compared with the anode, there has been less research on the direct involvement of solvents in the interphase formation on the cathode (8, 15, 16, 32). The connections between voltageinduced degradation, cathode interphase formation and evolution, and electrolyte-electrode reactions remain largely unexplored. To understand the potential-related transformation of cathodes, electrochemical and x-ray studies were conducted with 60-nm fully lithiated NMC532 films (fig. S12). One film was charged to 4.26 V with a constant current of 40 nA

Fig. 2. Solvent and lithiation state effects on the chemical reactions between cathode surface and electrolyte. (A and B) XANES of partially lithiated (Li $_{0.7}$ Ni $_{0.5}$ Mn $_{0.3}$ Co $_{0.2}$ O $_2$) (A) and fully lithiated films (LiNi $_{0.5}$ Mn $_{0.3}$ Co $_{0.2}$ O $_2$) (B) at the Ni K-edge in a total-reflection geometry with and without a 2-hour exposure to solvents (EC-EMC) or electrolyte (EC-EMC and LiPF $_6$ salt). (**C** and **D**) Visualizations of the interfacial H transfer and the associated reaction energy in solvents EMC (C) and EC (D) to form corresponding vinyl species and transfer two H to the Li $_{0.5}$ Ni $_{0.5}$ Mn $_{0.3}$ Co $_{0.2}$ O $_2$ (018) surface. (018) is the preferred orientation for NMC532 films grown on SrTiO $_3$ (110).

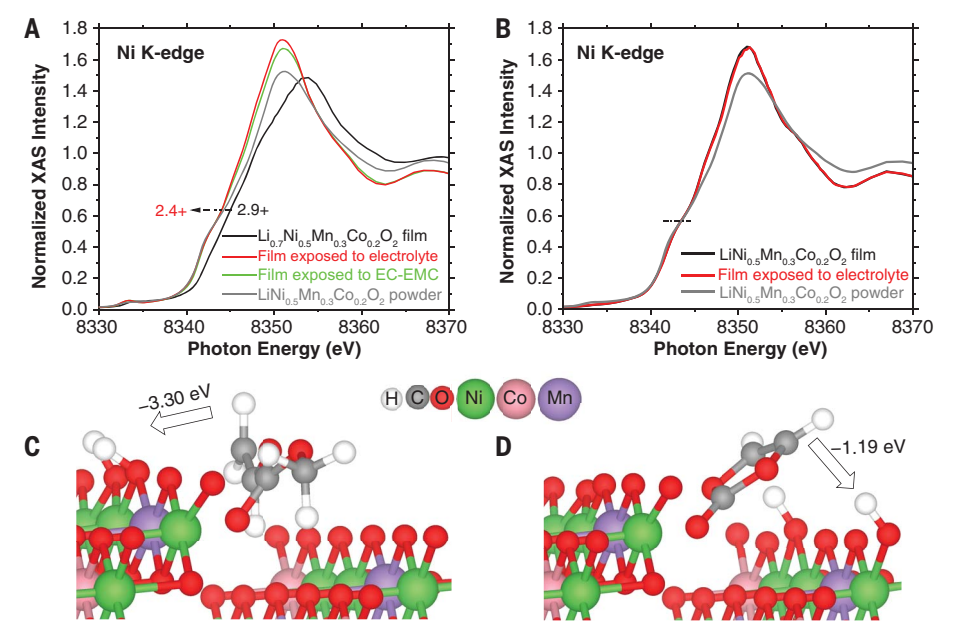
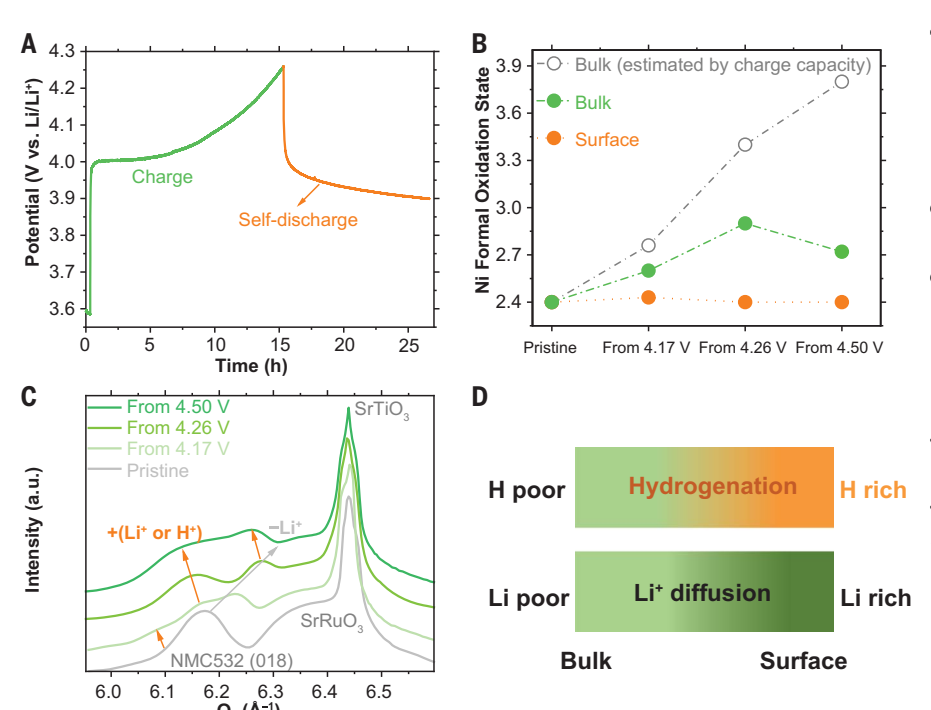


Fig. 3. Transformation of self-discharged NMC532 films. (A) Charge and self-discharge voltage-time curve of NMC532 film with a cutoff potential of 4.26 V. (B) Evolution of Ni oxidation states on surface (orange circles) and in bulk (green circles) in a pristine film and films that were fully relaxed from different potentials. The gray circles present the average Ni valence estimated by the charging capacity. (C) Synchrotron XRD profile around SrTiO₃ (004) Bragg peak for pristine and selfdischarged films. The gray and orange arrows indicate lattice contraction from delithiation and lattice expansion from hydrogenation or lithiation, respectively. Here, Qz is the scattering vector. (D) Schematic of vertical heterogeneity development in bulk and on surface, which can be driven by either H transfer-induced hydrogenation (top) or Li⁺ diffusion (bottom).



(~0.03 C) in a customized cone-type cell (see experimental section in the supplementary materials), and the OCV was monitored over time (materials and methods). The OCV dropped quickly in the initial 2 hours, then gradually stabilized over the course of 10 hours. Figure 3B shows the oxidation states of the electrode bulk and surface after this self-discharge. These data reveal an average oxidation state of Ni^{2.9+} in bulk and Ni^{2.4+} on surface. Only small changes were observed for Co and Mn within films (fig. S13). This difference in Ni oxidation states in

the surface and bulk is also observed at other cutoff potentials. Figure 3C shows x-ray diffraction (XRD) data of the films. With delithiation and self-discharge, the (018) peak in the pristine film splits into two broader peaks. At high Q, a substantial positive shift of the (018) peak indicates a lattice contraction due to delithiation (7). At lower Q, another broader XRD peak simultaneously appears, slightly shifting toward lower values with increased cutoff potential. Figure S14 shows the d-spacing of these peaks. From the XRD data together

with x-ray absorption spectroscopy (XAS) studies on surface and in bulk, we infer that the high-Q peak is from the delithiated bulk of the thin film, and the low-Q peak is attributable to a surface region with expanded lattice that results from ion insertion-induced chemical expansion (7, 33), forming reduced cathodes.

The surface and bulk regions differ in lattice expansion and oxidation states depending on the self-discharge conditions. These differences were much smaller at the 4.17-V cutoff

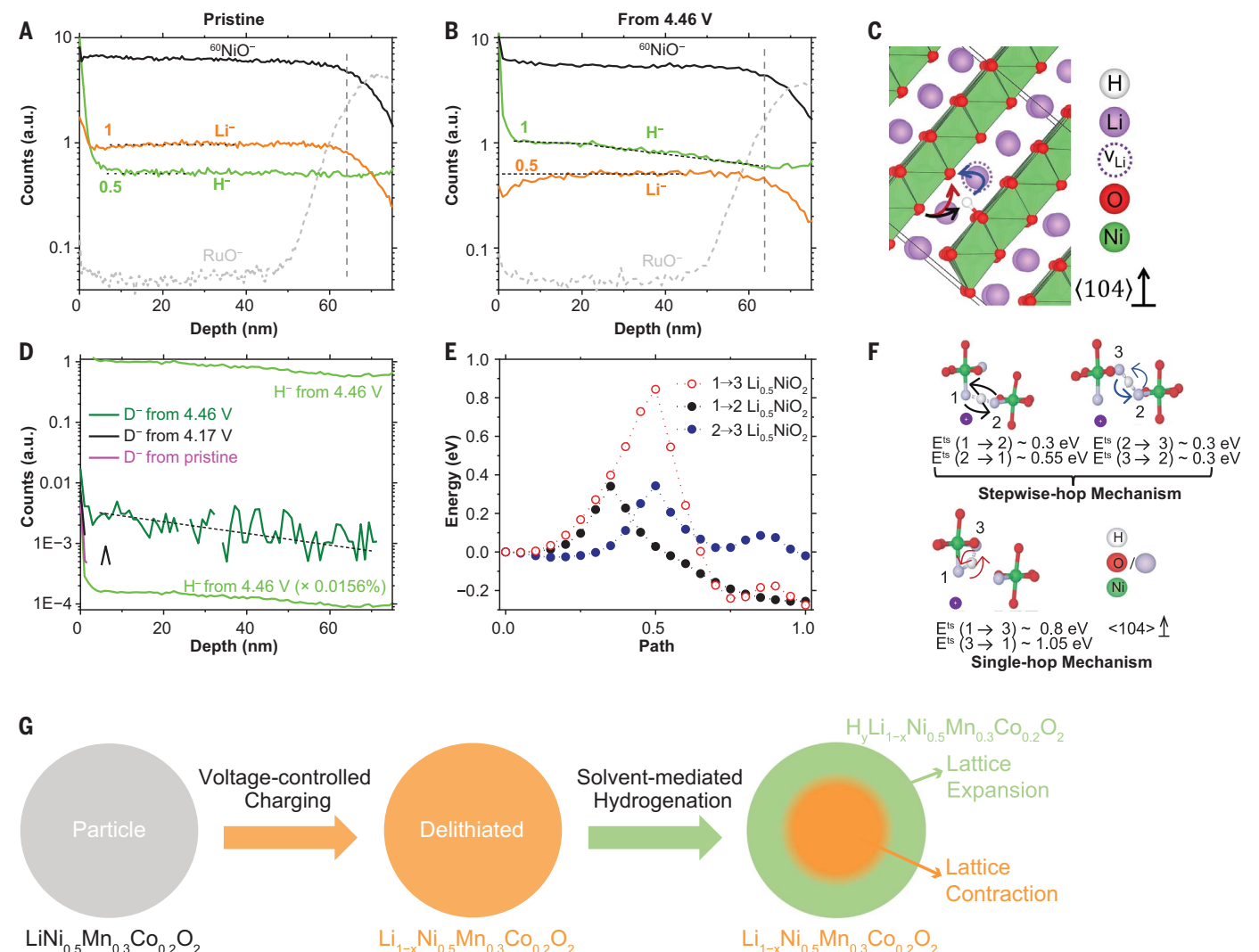


Fig. 4. Cathode hydrogenation and the TOF-SIMS depth profiles. (A and B) Depth profiles of negative ions 60 NiO $^-$, Li $^-$, and H $^-$ from the pristine NMC film (A) and after self-discharge from 4.46 V (B), which represent the corresponding elements Ni, Li, and H (RuO $^-$ is from the SrRuO $_3$ layer). (**C**) Two proton diffusion paths in Li $_{0.5}$ NiO $_2$ that involve a two-step hop between interlayer lattice oxygen (black and blue arrows) and a single hop (red arrow) within the layer. (**D**) Potential-dependent depth profiles of D $^-$ and H $^-$ signals for 4.46-V charged film (D's natural abundance ratio is 0.0156%). All signals have been normalized by the depth profiles of 18 O $^-$, which represent that of the whole film

(black dashed lines are for guiding the eyes, and the discontinuity in lines is because some D signals are below the detection threshold). (\mathbf{E}) Energy profiles of the two proton diffusion paths in (C). Compared with the single hop from position 1 to position 3, the stepwise hops from position 1 to position 2 and from position 2 to position 3 show decreased energy barriers. (\mathbf{F}) Visualization and energy of transition state (\mathbf{E}^{ts}) of stepwise-hop versus single-hop mechanisms for proton transport in $\mathrm{Li}_{0.5}\mathrm{NiO}_2$. The (104) orientation is used in (C) and (F) for clarity. (\mathbf{G}) Schematic of the chemo-mechanical coupling in layered cathodes particles involving both delithiation and hydrogenation.

compared with the 4.26-V cutoff (Fig. 3, B and C, and fig. S15). At 4.17 V, we observe Ni^{2.6+} in the bulk and an associated lithiation-induced lattice contraction. On the surface, however, we observe an average oxidation state of Ni^{2.43+} and a slightly expanded lattice (Fig. 3, B and C). Furthermore, when the cutoff potential is 4.5 V, which is outside the stability window of the electrolyte (figs. S16 and S17), the surface Ni in the self-discharged film was in a reduced state (2.4+) (Fig. 3B and fig. S18). As compared with 4.17 V, the XRD suggested an increased proportion of the surface reduced phase, as evidenced by the larger shoulder at low Q (Fig. 3C and fig. S14). In addition, the

XRD profiles show that the reduced phase peak becomes much broader at the 4.5-V cutoff, which is because of a larger d-spacing distribution or finite size effect. It is known that ion insertion–induced chemical expansion effects in oxides differ between Li⁺ and H⁺ (7). Thus, the negative shifts of low-Q Bragg peaks support the inference that self-discharge results in a surface region with an accumulation of H.

To further understand the origin of the surface reduction phase in self-discharged 60-nm ${\rm LiNi_{0.5}Mn_{0.3}Co_{0.2}O_2}$ films, element-specific depth profiles were conducted with time-of-flight secondary ion mass spectrometry (TOF-SIMS)

(34). Although the dehydrogenation of EMC is possible and suggested in our DFT studies, most current literature proposes that EC is the primary component that is oxidized in mixed solvents (19, 21, 35). To test this hypothesis, we turned to the fully deuterated EC (EC-D4) with both $\rm CH_2$ groups replaced by $\rm CD_2$. EC-D4 was dried and then mixed with the EMC solvent and salt to prepare the LP57 electrolyte. NMC532 films were charged to 4.17, 4.30, and 4.46 V and then held at OCV while the potential was monitored (fig. S19). The H signals on the top surface in the pristine film likely come from the surface hydrogen-containing layer (16), such as bicarbonate and adsorbed organic species,

in a thickness of a few nanometers (Fig. 4A and fig. S12), which did not lead to any observable surface reduction upon soaking (Fig. 2B). Metal oxide TOF-SIMS signals share similar intensity profiles in the pristine and selfdischarged films (Fig. 4, A and B, and fig. S20) and are consistent with our expectation that the thin-film matrix remains largely unchanged. On the basis of the prevailing self-discharge model, the diffusion of Li⁺ into the delithiated cathode should result in more Li⁺ present near the surface. However, within 20 nm of the NMC surface, the Li signal intensity is lower than that in the rest of the film, and a gradient exists toward the bulk (Fig. 4B); the Li signals decrease ~50% on average in the self-discharged NMC532, close to the expected half-delithiated state in the bulk. Deuterium (D) was detected through D signals in the film above its natural abundance (Fig. 4D). This confirms that D from the CD₂ groups in EC-D4 is inserted into the film and builds a small concentration gradient consistent with the transfer mechanism (Fig. 2D) but with a very limited amount (about 0.2% of H).

Relative to the pristine film, there is an average enhancement of 50% for H signal in the top 30 nm, which suggests a 50% increase of protons near the film surface. Additionally, a decreasing hydrogen content gradient builds up from surface to bulk, which is opposite to the Li⁺ gradient (Fig. 4B). Such Li/H gradients have not been observed when the pristine film was soaked in the same electrolyte for 85 hours (fig. S21B). The TOF-SIMS data suggest that EMC is the primary source for protons within thin films. These observations are consistent with studies that show that EMC and DEC (which are structurally similar) show lower resistance toward oxidation compared with EC (36, 37), although some past work only implicates EC in the solvent oxidation (19, 21, 35). When pure EMC was used as the solvent for $LiPF_6$, a similar voltage drop was found (fig. S22). Combining the direct evidence on D transfer from EC-D4 to cathodes (Fig. 4D) and noting that the C-D bond is stronger than the C-H bond, our data suggest that CH2-containing carbonate solvents, EC and EMC, can both be the source of H in delithiated cathodes. Our results suggest that EMC can be more prone to H transfer and to the transfer of protons and electrons to the oxide. This aligns well with a study of the detection of VC from the dehydrogenation of EC in an electrolyte where the CH₂-free dimethyl carbonate (DMC) replaced the EMC (22). The Li⁺ gradient was also observed with a lower cutoff potential (4.17 V), whereas both D and H are much lower (fig. S21A). The existence of a Li-depletion layer (38) and a Ni-reduction surface (9, 15, 27) have both been evidenced on a variety of cycled NMC particles, which cannot be explained by existing models. Surface hydrogenation offers the following explanation for these phenomena (Fig. 4G).

$$\text{LiNi}_{0.5}\text{Mn}_{0.3}\text{Co}_{0.2}\text{O}_2 \rightarrow \\ \text{Li}_{1-x}\text{Ni}_{0.5}\text{Mn}_{0.3}\text{Co}_{0.2}\text{O}_2 + x(\text{Li}^+ + e^-)$$
 (1)

$$CH_3O(C = O)OCH_2CH_3 \rightarrow CH_3O(C = O)OCH = CH_2 + 2(H^+ + e^-)$$
 (2)

$$\text{Li}_{1-x}\text{Ni}_{0.5}\text{Mn}_{0.3}\text{Co}_{0.2}\text{O}_2 + y(\text{H}^+ + \text{e}^-) \rightarrow H_y\text{Li}_{1-x}\text{Ni}_{0.5}\text{Mn}_{0.3}\text{Co}_{0.2}\text{O}_2$$
 (3

Combining studies of cathodes in both commercial powders and model films and surfacesensitive x-ray spectroscopy and scattering with the depth profile and isotopically labeled mass spectroscopic characterizations in conjunction with computation and modeling, our study shows that hydrogen transfer occurs from carbonate solvent to delithiated cathode. Increasing the cutoff potential removes more Li⁺ and oxidizes Ni in the bulk cathode, and the carbonate solvents then become more prone to interfacial H transfer on the delithiated surfaces (Eq. 1 and Fig. 4G). This can be rationalized by two successive steps with EMC as an example: (i) Two H atoms are stripped from EMC on the delithiated cathode surface, producing protons plus electrons and leaving vinyl species, such as methyl vinyl carbonate, that are soluble in the carbonate electrolyte (Eq. 2). (ii) Electrons transfer to the TM oxide, reducing Ni, and protons are transferred to the oxygen ligand (Eq. 3). Further thermodynamic analysis confirms that the equilibrium potential of a cell is influenced by the ratio of hydrogenation (y) and delithiation (x) (supplementary text), which is essential to understanding the impact of the hydrogenation of delithiated cathodes on voltage fade.

Transport pathways of protons and the implications of cathode hydrogenation

Our results suggest that proton transport on cathode surface is initiated by the TM-mediated H transfer (Fig. 2, C and D) and facilitated by the presence of an increased proportion of Li⁺ vacancies and increased proton concentration (Fig. 4D and fig. S21A). The proton diffuses into the cathode by hopping between neighboring oxygens (39). Using Li_{0.5}NiO₂ as a model, proton diffusion was modeled as either a stepwise hopping mechanism $(1\rightarrow 2, 2\rightarrow 3)$ with barriers of ~0.3 eV each or as a single hop $(1\rightarrow 3)$ with a barrier of ~ 0.8 eV (Fig. 4, C and F, and fig. S23). Position 1 is adjacent to an occupied Li⁺ site in the lattice, whereas position 3 has no Li⁺ in an adjacent site. Li⁺ diffusion barriers range from ~0.3 eV in Li_{0.5}NiO₂ to ~0.6 eV in LiNiO₂ (fig. S24). However, the barriers for Li⁺ and H⁺ diffusion are sensitive to the local environment because of the Coulombic repulsion between cations occupying the adjacent sites. Consequently, the barriers for H⁺ diffusion along paths $(3\rightarrow 1)$ and $(2\rightarrow 1)$ are ~1.05 eV and ~0.55 eV, respectively. A similar effect is observed for Li⁺ diffusion paths as well. The persistent proton gradients can be attributable to the low diffusivity of protons in oxides (39). As known in chemo-mechanics, nanoscale intraparticle inhomogeneities in composition often induce mechanical strain and fracture, thus degrading ion insertion materials (7), and have been widely reported in all layered cathodes (7, 15). The prevailing understanding is that this is because of the inhomogeneities in lithiation state (17) and/or the reconstruction of cathode surface (9). On the basis of our experimental results, rock salt NiO is excluded as the main phase of the surface reduction regions in self-discharged films (supplementary text). We speculate that the surface hydrogenated phase, which has a larger lattice parameter than the bulk delithiated oxide, may influence the chemo-mechanical couplings that affect the structural stability of cathodes (Fig. 4G).

For decades, cathode protonation (40) and electrolyte degradation (5, 19, 20, 22, 35) have been debated. Carbonate solvents are dominant components in present LIB electrolytes and can generate protons by H transfer on delithiated cathode surfaces. Such a high local $H (H^+ + e^-)$ concentration near the cathode surface is critical for oxide hydrogenation; thus, the solvent dehydrogenation can serve as a principal local proton source. Our model also explains the protonation of layered oxides that underwent chemical delithiation in carbonate solvents (41). Trace water in the electrolyte could offer another proton source, but the moisture content in as-dried solvent is very low [~2 parts per million (ppm); experimental section in the supplementary materials]. The BDE of C-H in the CH₂ group of carbonate solvents (around 370 kJ/mol) is much lower than that of O-H in H₂O (458.9 kJ/mol). This suggests that the local concentration of moisturerelated protons on the cathode surface is dilute. When the cathode is discharged, protons within the cathode surface region can escape and diffuse into the electrolyte, resulting in further (electro)chemical processes. For example, protic species originating at the cathode were observed to diffuse to the anode, releasing H2 (42). CH₂ groups can be found in a variety of battery electrolyte solvents, including partially fluorinated carbonates (fig. S25). Partially fluorinated solvents only elicit a minor mitigation in OCV decreases when compared with carbonate solvents (fig. S26). This supports our model that the CH₂ group is the primary source of the transferred H. Recent findings on OCV drop mitigation using CH2-free additives further support this picture (12).

Along with calendar life, the effect of selfdischarge on the electrochemical performance of NMC532 electrodes was also investigated (fig. S27). We observed that the 100-hour self-discharge process showed an insignificant impact on short-term capacity retention. However, it consistently reduced the average discharge potential of the cells, presuming that the inserted protons lead to the reduction of the average valence of TMs and hence the thermodynamic electrochemical potential of Li⁺ in the oxide framework. This study illustrates the role of hydrogen as a redox mediator from solvent dehydrogenation and the potential impact of chemical hydrogenation on electrochemical behavior.

Beyond the Ni redox, the concept of solvent-mediated cathode hydrogenation may be broadly applicable to other layered cathode oxides, such as Li_xCoO_2 (41), Li-rich cathodes, and sodium layered TM oxides (Na_xTMO_2), where high-valent surface TMs interact with carbonate solvents. On the basis of the insight that we obtained into degradation mechanisms, we hypothesize that lower cutoff voltages, CH_2 -free additives added to the electrolyte, and surface coating of the cathode will reduce the active surface TMs that are exposed to carbonate solvents. These approaches can thus mitigate self-discharge and cathode degradation in electrolytes.

REFERENCES AND NOTES

- 1. N. Lu et al., Nature **546**, 124-128 (2017).
- 2. Y. Zhou et al., Nature **534**, 231–234 (2016).
- G. J. Choi, Q. Zhu, D. C. Miller, C. J. Gu, R. R. Knowles, *Nature* 539, 268–271 (2016).
- 4. M. S. Whittingham, Science 192, 1126-1127 (1976).
- 5. K. Xu, Chem. Rev. **104**, 4303–4418 (2004).
- J. L. Dempsey, J. R. Winkler, H. B. Gray, Chem. Rev. 110, 7024–7039 (2010).
- 7. S. R. Bishop et al., Annu. Rev. Mater. Res. 44, 205–239 (2014).
- 8. J. M. Tarascon, M. Armand, Nature 414, 359–367 (2001).
- 9. C. Xu et al., Nat. Mater. 20, 84-92 (2021).
- 10. Y.-K. Sun et al., Nat. Mater. 8, 320–324 (2009).
- 11. D. Aurbach, J. Power Sources 89, 206-218 (2000).
- D. S. Hall, T. Hynes, J. R. Dahn, J. Electrochem. Soc. 165, A2961 (2018).

- 13. H. A. Andreas, J. Electrochem. Soc. 162, A5047 (2015).
- K. Mizushima, P. C. Jones, P. J. Wiseman, J. B. Goodenough, Mater. Res. Bull. 15, 783–789 (1980).
- 15. H. Y. Asl, A. Manthiram, Science 369, 140-141 (2020).
- Y. S. Meng, V. Srinivasan, K. Xu, Science 378, eabq3750 (2022).
- 17. M. D. Radin et al., Adv. Energy Mater. 7, 1602888 (2017).
- Y. Ozawa, R. Yazami, B. Fultz, J. Power Sources 119–121, 918–923 (2003).
- S. Xu et al., ACS Appl. Mater. Interfaces 9, 20545–20553 (2017).
- 20. Z. Chen, Chem. Commun. 58, 10127-10135 (2022).
- Y. Zhang et al., Energy Environ. Sci. 13, 183–199 (2020).
 B. L. D. Rinkel, J. P. Vivek, N. Garcia-Araez, C. P. Grey, Energy Environ. Sci. 15, 3416–3438 (2022).
- B. L. D. Rinkel, D. S. Hall, I. Temprano, C. P. Grey, J. Am. Chem. Soc. 142, 15058–15074 (2020).
- T. Toma, R. Maezono, K. Hongo, ACS Appl. Energy Mater. 3, 4078–4087 (2020).
- S. Posada-Pérez, G.-M. Rignanese, G. Hautier, Chem. Mater. 33, 6942–6954 (2021).
- L. Hartmann, D. Pritzl, H. Beyer, H. A. Gasteiger, J. Electrochem. Soc. 168, 070507 (2021).
- 27. R. Qiao et al., J. Power Sources 360, 294-300 (2017).
- 28. Y. Yu et al., ACS Appl. Mater. Interfaces 12, 55865–55875 (2020).
- D. Takamatsu et al., Angew. Chem. Int. Ed. 51, 11597–11601 (2012).
- 30. S. J. Blanksby, G. B. Ellison, Acc. Chem. Res. 36, 255-263 (2003).
- 31. J. M. Mayer, Acc. Chem. Res. 44, 36-46 (2011).
- 32. J. Langdon, A. Manthiram, *Adv. Funct. Mater.* **31**, 2010267–2010275 (2021).
- G. Wan, C. J. Sun, J. W. Freeland, D. D. Fong, Acc. Chem. Res. 54, 3039–3049 (2021).
- 34. Y. Zhou et al., Nat. Nanotechnol. 15, 224-230 (2020).
- T. M. Østergaard et al., J. Phys. Chem. C 122, 10442–10449 (2018).
- J. M. Tarascon, D. Guyomard, Solid State Ion. 69, 293–305 (1994).
- K. Xu, S. P. Ding, T. R. Jow, J. Electrochem. Soc. 146, 4172 (1999).
- 38. S. Li et al., Nat. Commun. 11, 4433 (2020).
- T. Norby, Y. Larring, Curr. Opin. Solid State Mater. Sci. 2, 593–599 (1997).
- R. Benedek, M. M. Thackeray, A. van de Walle, *Chem. Mater.* 20, 5485–5490 (2008).
- 41. J. Choi, E. Alvarez, T. A. Arunkumar, A. Manthiram, Electrochem. Solid-State Lett. 9, A241 (2006).
- M. Metzger, B. Strehle, S. Solchenbach, H. A. Gasteiger, J. Electrochem. Soc. 163, A798 (2016).

ACKNOWLEDGMENTS

- G.W. acknowledges helpful discussions with P. Frank,
- C. E. D. Chidsey, D. D. Fong, and Q. Zhu; inspiration and support from
- P. A. Pianetta and A. Majumdar; and setup help from Y. D. Zhou,
- R. Arthur, J. W. Freeland, and D. Nordlund. The authors dedicate

this research work to the memory of George Crabtree and Peter Faguy for their years of inspiration and dedication to the battery community. Funding: This work was supported by the Vehicle Technologies Office, funded by the Office of Energy Efficiency and Renewable Energy, US Department of Energy (DOE), including Interagency Agreement IAA 89243322SEE000018 to Army Research Laboratory. The work used DOE Office of Science User Facilities, Advanced Photon Source (no. DE-ACO2-06CH11357), Stanford Synchrotron Radiation Lightsource (no. DE-AC02-76SF00515), Environmental Molecular Sciences Laboratory (EMSL) (grid 436923.9, no. 10.46936/sarr.proj.2018.50242/ 60006384), and Stanford Nano Shared Facilities (National Science Foundation award ECCS-2026822). TOF-SIMS and data analysis performed using EMSL were supported by the DOE, Office of Science, Office of Basic Energy Sciences, Division of Materials Sciences and Engineering under award no. 10122. K.X. thanks the Joint Center of Energy Storage Research, an energy hub funded by the US DOE Basic Energy Science, for support. C.-C.C. acknowledges support from the Ministry of Science and Technology of Taiwan (nos. MOST 110-2628-E-002-009 and 111-3116-F-011-006) and the Yushan Young Fellow Program, Ministry of Education of Taiwan (MOE-109-YSFEE-0003-002-P1). J.F. acknowledges support from European Union Horizon 2020 under the Marie Sklodowska-Curie grant. Z.F. acknowledges support from the US National Science Foundation (nos. CBET-1949870 and CBET-2016192) and help from M. Wang and A. Sokolov. G.W. acknowledges assistance from J. E. Mars. C. Cao. and C. J. Takacs. Author contributions: G.W., K.X., O.B., H.-G.S., and M.F.T. conceived the collaboration project. G.W., T.P.P., and C.-C.C. conceived the design and concept of the study and interpreted the data. G.W., C.-C.C., Y.Z., Z.C., J.C., M.A.S., and K.X. designed and conducted the electrochemical studies. G.W., Z.Zha., C.-J.S., and S.K. conducted x-ray studies and analyzed the results, T.P.P. conducted DFT with suggestions from O.B., and Z.Zhu, S.P.H., G.W., and Y.D. conducted TOF-SIMS studies, L.M. and M.A.S. prepared electrolyte and solvent. Z.F. and J.F. conducted film growth G.W., T.P.P., C.-C.C., M.A.S., Z.Zhu, Y.Z., M.F.T., and K.X. wrote the manuscript with input from all authors. G.W. led and coordinated the project and manuscript preparation with suggestions from O.B., M.F.T., and K.X. Competing interests: The authors declare that they have no competing interests. Data and materials availability: All data are available in the main text or the supplementary materials. License information: Copyright © 2024 the authors, some rights reserved; exclusive licensee American Association for the Advancement of Science. No claim to original US government works, https://www. science.org/about/science-licenses-journal-article-reuse

SUPPLEMENTARY MATERIALS

science.org/doi/10.1126/science.adg4687 Materials and Methods Supplementary Text Figs. S1 to S27 References (43–68)

Submitted 3 January 2023; accepted 2 August 2024 10.1126/science.adg4687